processes

MDPI

Article

Fracture Geometry Modeling and Analysis of Layer-Crossing Conditions in Continental Shale Considering Apparent Fracture Toughness

Luopeng Li [1], Huanqiang Yang [2,*] and Donghang Li [3]

[1] School of Petroleum Engineering, China University of Petroleum (East China), Qingdao 266580, China; 20130079@upc.edu.cn
[2] School of Petroleum Engineering, Yangtze University, Wuhan 430100, China
[3] School of Geosciences, Yangtze University, Wuhan 430100, China; lidonghang@yangtzeu.edu.cn
* Correspondence: yanghuanqiang@yangtzeu.edu.cn

Abstract

Vertical viscous resistance and bedding deformation jointly influence hydraulic fracture propagation in continental shale. A coupled pseudo-three-dimensional (P3D) framework incorporates apparent fracture toughness (effective front toughness accounting for vertical viscous resistance) and tangential bedding compliance. Near-tip aperture matching yields an implicit toughness equation with a unique nonnegative root. A layered elastic weak form, fluid conservation, and front updates couple pressure, aperture, and interfacial displacement. A vertical propagation pressure relation is derived at a prescribed height for perfectly bonded conditions with symmetric stress barriers. Existing end-of-treatment data for stage 8 of a Sichuan Basin well are reanalyzed. The modified scheme yields an average height of 55.6 m, within the interpreted 52–58 m range, and a half-length of 178 m, deviating 3.49% from the interpreted 172 m. Increasing prescribed additional toughness from 0.1 to 0.7 MPa·m$^{1/2}$ reduces average height and half-length by 38.62% and 22.22%, respectively, while maximum tangential interfacial displacement increases from 0.41 to 1.26 mm. The framework clarifies the distinct roles and coupling of propagation resistance and elastic bedding deformation, providing theoretical and case-based support for fracture height control, geometry analysis, and assessment of layer-crossing conditions.

Keywords: continental shale; hydraulic fracturing; apparent fracture toughness; pseudo-three-dimensional model; bedding interface; layer-crossing conditions

Check for updates

Academic Editor: Dicho Stratiev

Received: 27 September 2026
Revised: 17 October 2026
Accepted: 20 October 2026
Published: 26 October 2026

Copyright: © 2026 by the authors. Licensee MDPI, Basel, Switzerland. This article is an open access article distributed under the terms and conditions of the Creative Commons Attribution (CC BY) license.

1. Introduction

Continental shale oil in China occurs in diverse forms, and its development requires consideration of variations in reservoir composition and heterogeneity [1]. Vertical hydraulic fracture growth directly affects the extent of reservoir stimulation and the degree of fracture containment within the target interval. Bedding, natural fractures, and other geological discontinuities can alter fracture propagation paths, fluid movement, and proppant transport, producing fracture geometries that differ from idealized predictions for homogeneous media [2]. Fracture-height analysis in layered formations therefore needs to account for interlayer stress contrasts, rock fracture properties, and interface mechanical responses.

Hydraulic fracture propagation involves coupled mechanisms of rock deformation, flow within the fracture, fracture processes, and fluid leakoff; their relative contributions govern propagation behavior [3,4]. Various numerical methods have been developed to

address this problem, and their applicability depends on the physical processes represented, fracture geometry complexity, and validation conditions [5]. Settgast et al. developed a fully coupled three-dimensional method combining finite element discretization of the solid with finite volume discretization of the flow [6]. The extended finite element work of Moës and Belytschko provided a methodological basis for cohesive crack calculations in which crack paths need not conform to mesh boundaries [7]. Peirce and Detournay combined near-tip asymptotic relations with an implicit level set method to track hydraulic fracture fronts [8]. Damjanac and Cundall used distinct element methods to investigate hydraulic fracturing in naturally fractured reservoirs [9]. These approaches provide different routes to complex fracture simulation and demonstrate the need to interpret model results in light of their physical assumptions and validation conditions.

Pseudo-three-dimensional (P3D) models approximate a three-dimensional fracture using local vertical cross-sections distributed along the propagation direction, reducing computational complexity while retaining variations in fracture height. Classical P3D models generally assume local plane-strain elasticity and uniform pressure within each cross-section, and represent stress-barrier effects on vertical propagation through an equilibrium-height relation [10]. To approximate viscous effects associated with vertical flow, Dontsov and Peirce proposed an enhanced P3D model incorporating an apparent-toughness correction, together with nonlocal elasticity and lateral fracture toughness [11]. Related work also showed that toughness criteria for lateral propagation must be consistent with the adopted elastic approximation [12]. Apparent toughness should therefore be understood as an effective correction associated with a particular propagation state and calibration, with a physical meaning distinct from the material fracture toughness of the rock.

In this study, apparent fracture toughness comprises the material fracture toughness K_{IC} and an additional term ΔK_v. The latter represents, in toughness units, the vertical viscous resistance not explicitly resolved under the P3D assumption of uniform cross-sectional pressure. It varies with fluid viscosity, propagation speed, elastic properties, and matching length, and is therefore an effective quantity dependent on the propagation state. In contrast, K_{IC} characterizes the intrinsic fracture resistance of the rock. Here, ΔK_v does not replace K_{IC}, and tangential elastic energy stored at bedding interfaces is not included in this viscous contribution.

The effects of bedding interfaces also involve distinct mechanisms. Schoenberg's linear slip interface theory describes interface compliance through a relation between traction and displacement jump, providing a basis for idealized elastic interface models [13]. Peirce et al. subsequently investigated layered fracture models in which linear springs control relative interlayer shear deformation and applied them to P3D analysis [14]. When fracture penetration across an interface or deflection along it is considered, competition between fracture paths must also be included. He and Hutchinson studied crack deflection at interfaces between dissimilar materials by comparing energy release rates with the corresponding fracture resistances [15]. Yang and Zhao combined finite element analysis with energy release rate calculations to investigate vertical fracture penetration and deflection at coal–mudstone interfaces [16].

For interface problems involving friction and fluid action, Zhang and Jeffrey showed that bedding-interface slip, fluid redistribution, and new fracture initiation jointly influence the reinitiation or termination of fluid-driven fractures [17]. Lu et al. used layered specimens to demonstrate the effects of weak interfaces and layered material properties on fracture containment and height growth [18]. More recently, Zeng et al. analyzed hydraulic fracture interactions with bedding planes using a three-dimensional coupled model [19]; Shi et al. investigated hydraulic fracturing responses in laminated shale with different bedding configurations [20]; and Li et al. coupled frictional bedding slip with

hydraulic fracture propagation to examine its effects on fracture geometry [21]. These studies indicate that elastic interface deformation, frictional slip, and interface fracture have distinct governing relations, and their physical meanings should be identified separately in simplified models.

From the perspective of propagation mechanisms, Huang et al. [22] used a two-dimensional discrete element method to examine the effects of interlayer stiffness ratios, toughness ratios, and stress contrasts on fracture height growth. Their results showed that layer-crossing behavior is closely related to whether propagation is viscosity- or toughness-dominated. Huang et al. [23] further investigated inherent rock heterogeneity and grain size, showing that heterogeneity can alter net fracture pressure, tortuosity, and effective fracture resistance. These studies demonstrate that interpretations of geometry changes and "effective toughness" must be tied to the specific mechanisms involved. The additional apparent toughness in this study refers specifically to the vertical viscous correction, whereas bedding compliance enters through the cross-sectional elastic relations. Both have physical origins distinct from the effective toughness associated with grain-scale heterogeneity.

Building on these studies, this work incorporates the apparent-toughness correction for vertical viscous resistance and tangential elastic compliance of bedding interfaces into a single P3D formulation. It identifies their respective roles in the front conditions and pressure–aperture mapping, establishes the nonnegative-root properties of the implicit toughness update, presents the layered elastic weak form and its discretization, and derives a propagation pressure condition for a reference problem with symmetric stress barriers. Existing end-of-treatment cases and field interpretations are then used for geometry comparisons and parameter-trend analysis. In relation to studies focusing on discrete fracture paths, interface friction, or grain-scale heterogeneity, this work examines the connection between resistance correction and elastic interfaces within a simplified P3D framework, and its implications for fracture geometry and layer-crossing conditions.

2. Fracture Parameter Model

2.1. Geometry and Basic Assumptions

A vertical hydraulic fracture with two symmetric wings is considered. The x-direction denotes horizontal propagation, z is vertical, and y is the aperture direction; horizontal bedding planes are parallel to the x–y plane. The fracture half-length is $L(t)$, the local full height is h(x,t), and the aperture is $w(x,z,t)$. In the reference problem, the upper and lower fronts are symmetric about the midplane of the injection layer and lie at $z = \pm h/2$. The injection-layer thickness H_p is a fixed geological input. Figure 1 shows the side-view outline and the aperture cross-section at a fixed x.

Each rock layer is assumed to exhibit small-strain, isotropic linear elasticity, with material constants that may differ between layers. The fluid is treated as incompressible and Newtonian, with uniform pressure within each local cross-section. The reference description neglects gravity-induced vertical pressure differences, fluid lag, and proppant transport. A local cross-sectional approximation is used along x, with displacements in the y–z plane as the elastic unknowns. This dimensional reduction does not retain the full three-dimensional elastic interactions.

In situ compressive stress is taken as positive. Fluid pressure p_f and net pressure p_n satisfy

$$p_n(x,z,t) = p_f(x,t) - \sigma_h(z),\ \sigma_h(z) = \sigma_1 + \Delta\sigma\chi_b(z) \quad (1)$$

Here, $\Delta\sigma = \sigma_2 - \sigma_1$; χ_b equals 0 within the injection layer and 1 within the symmetric upper and lower bounding layers. A general layered elastic problem may use a layer-specific stress profile $\sigma_h(z)$, whereas the quantitative calibration of the apparent-toughness

relation in Section 2.3 is restricted to the reference problem with symmetric stress barriers. The plane-strain modulus, viscosity parameter, and cross-sectional area are defined as

$$E'_\ell = \frac{E_\ell}{1-\nu_\ell^2}, \mu' = 12\mu, A(x,t) = \int_{-h/2}^{h/2} w(x,z,t)dz \tag{2}$$

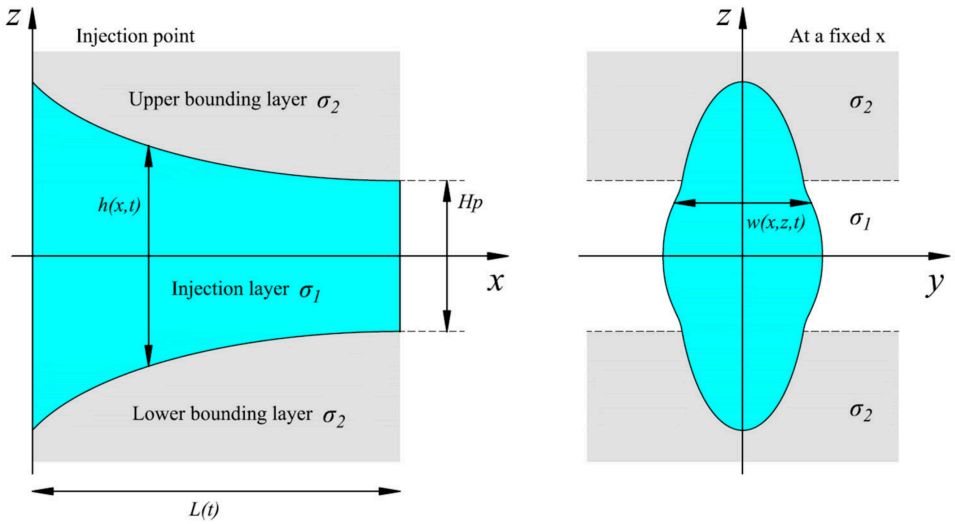


Figure 1. Geometry and aperture definitions for the reference P3D model. (**a**) Side view of the right fracture wing in the *x*–*z* plane, with injection at the left end; (**b**) *y*–*z* aperture cross-section at a fixed *x*. The blue-shaded regions represent the fracture extent in the *x*–*z* plane in (**a**) and the aperture cross-section between the two fracture faces in (**b**). The *x*-, *y*-, and *z*-directions denote horizontal propagation, aperture, and the vertical direction, respectively. Here, *h(x,t)* is the full fracture height, *L(t)* the half-length, H_p the injection-layer thickness, and *w(x,z,t)* the aperture between the two fracture faces. The minimum horizontal stresses in the injection layer and upper and lower bounding layers are σ_1 and σ_2, respectively. The outlines and aperture proportions are schematic and do not represent the actual mesh or relative layer thicknesses.

2.2. Elastic Opening and Reference Propagation Relations

Let a = h/2 denote the vertical fracture half-height. For a homogeneous reference cross-section with perfectly bonded interfaces, the local plane-strain elastic relation can be written as a singular integral [10]:

$$p_n(z) = \frac{E'}{4\pi} PV \int_{-a}^{a} \frac{\partial w(s)/\partial s}{z-s} ds \tag{3}$$

Here, PV denotes the Cauchy principal value, and x and t are omitted for brevity. The aperture vanishes at the upper and lower tips. This relation retains the effect of stress discontinuities without prescribing an elliptical aperture profile across layers. The mode I stress intensity factor at the upper tip of the reference cross-section is

$$K_I^+ = \frac{1}{\sqrt{\pi a}} \int_{-a}^{a} p_n(s) \sqrt{\frac{a+s}{a-s}} ds \tag{4}$$

The corresponding lower-tip expression is obtained by reversing the sign of s in the weight function. For a uniform net pressure p_n, the reference solution is

$$w(z) = \frac{4p_n}{E'} \sqrt{a^2 - z^2}, K_I = p_n \sqrt{\pi a} \tag{5}$$

The integral relations and analytical solution above provide checks for the perfectly bonded limit. When compliant interfaces are present, the aperture must be obtained from the layered problem in Section 2.4 rather than simultaneously imposing the elliptical profile in Equation (5). For a mode I tip located within a homogeneous layer and sufficiently far from material interfaces, K_I can also be extracted from the local aperture asymptote:

$$K_I = \frac{E'_{tip}}{8} lim_{s\to 0^+}\left[w(s)\sqrt{\frac{2\pi}{s}}\right] \quad (6)$$

Here, s is the distance from the tip, and E'_{tip} is the plane-strain modulus of the layer containing the tip. When the tip reaches an interface between dissimilar materials, the local singular field may change, so the homogeneous-tip relation cannot be applied unconditionally. Interface-crossing assessment requires the path and energy conditions discussed in Section 2.6.

2.3. Apparent Fracture Toughness and Its Implicit Update

Let K_{IC} and ΔK_v denote the material fracture toughness and additional apparent toughness, respectively. Their sum, K_{eff}, is the apparent fracture toughness and represents the effective resistance to be overcome by the vertical front under the present approximation:

$$K_{eff} = K_{IC} + \Delta K_v \quad (7)$$

The term ΔK_v converts the effect of the viscous pressure drop during vertical flow on tip propagation into a resistance term with the same dimensions as a stress intensity factor. Its value depends on the propagation speed and matching state, rather than being a fixed material constant. At a reference speed V = 0, the implicit relation gives $\Delta K_v = 0$, while the intrinsic material toughness K_{IC} remains. Thus, "zero additional toughness" means only that the viscous contribution vanishes.

The term ΔK_v approximates the vertical viscous resistance that is not explicitly resolved. If vertical lubrication flow is already fully computed, the same contribution should not be added again. Following the near-tip matching approach of Dontsov and Peirce [11], matching the toughness-dominated and viscosity-dominated aperture profiles at a characteristic distance d gives

$$\Delta K_v = \sqrt{\frac{\pi}{32}}\beta_m (E')^{2/3}(\mu')^{1/3}V^{1/3}d^{1/6},\ \beta_m = 2^{1/3}3^{5/6} \quad (8)$$

Here, V is the vertical propagation speed of an individual tip. The matching distance d is a characteristic model length, distinct from the actual thickness d_ℓ of layer ℓ in Figure 2. After absorbing the matching prefactor into the redefinition and calibration of the characteristic length, the approximate relation for symmetric stress barriers is [11]

$$r = C^{1/6}(\mu')^{1/3}(E')^{2/3}V^{1/3}h^{1/6}\left(1+\frac{C_2 H_p \Delta\sigma}{h^{1/2}r}\right)^{-1/6},\ r = \Delta K_v \quad (9)$$

In the original KGD reference calibration, C = 0.175 and 0.21 were used for distributed and point sources, respectively, and C_2 = 0.5 was used for the stress-barrier correction. These are literature calibration values rather than parameters refitted to the field case in this study. In Equations (8) to (10), E′ denotes the plane-strain modulus of the homogeneous reference problem and is not replaced by an uncalibrated average of layered moduli. The wellhead injection configuration for horizontal fracture propagation does not directly determine the equivalent source type in the vertical KGD problem. The applicability of this

approximation requires separate assessment when elastic mismatch or multiple compliant interfaces significantly affect the vertical aperture profile.

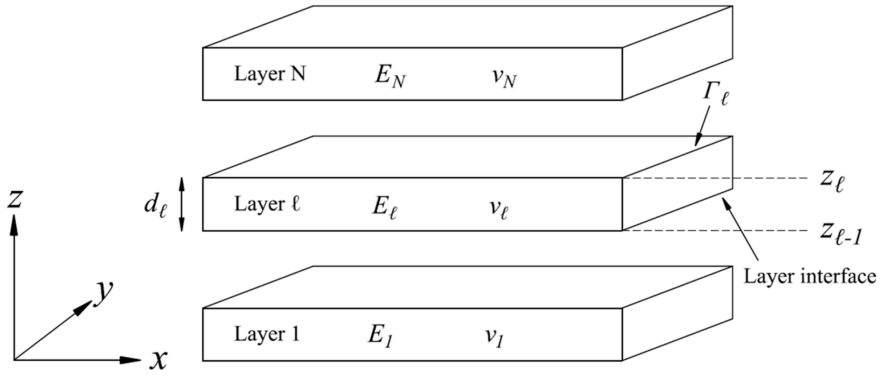


Figure 2. Geometry and parameter definitions for the layered medium. Layers are numbered from 1 to N from bottom to top. The script lowercase letter ℓ denotes an arbitrary layer and is distinguished from the digit 1. Layer ℓ lies between $z_{\ell-1}$ and z_ℓ; d_ℓ, E_ℓ, and ν_ℓ denote its thickness, Young's modulus, and Poisson's ratio, respectively, and Γ_ℓ denotes its upper internal interface. Coordinate directions are consistent with Figure 1. The schematic does not prescribe the actual number of layers, their thicknesses, or interface spacing.

Let B and F denote the barrier term and viscous driving term, respectively. Raising Equation (9) to the sixth power and rearranging gives

$$r^6 + Br^5 - F = 0,\ B = \frac{C_2 H_p \Delta\sigma}{h^{1/2}},\ F = C\left(\mu'\right)^2\left(E'\right)^4 V^2 h \tag{10}$$

For h > 0, $\Delta\sigma \geq 0$, and V > 0, B ≥ 0 and F > 0. The equation has a unique positive root in the interval from 0 to $F^{1/6}$; r = 0 is used when V = 0. Uniqueness of the positive root, dimensional consistency, and dimensionless sensitivity are discussed in Appendix B. For symmetric propagation of the upper and lower fronts, the implicit time update requires

$$V^{n+1} = max\left(0, \frac{h^{n+1} - h^n}{2\Delta t}\right) \tag{11}$$

Thus, r, h, and pressure are coupled unknowns. An increase in treatment duration alone does not establish a monotonic decrease in r, because r is jointly affected by fracture height, the stress barrier, and propagation speed.

2.4. Layered Elastic Interface Problem and Aperture Feedback

Figure 2 defines the parameters of the layered medium. The layers are numbered from 1 to N from bottom to top. The upper and lower boundaries of layer ℓ are located at z_ℓ and $z_{\ell-1}$, respectively, and its thickness is $d_\ell = z_\ell - z_{\ell-1}$. The internal interface Γ_ℓ lies at the upper boundary of layer ℓ, whose material properties are E_ℓ and ν_ℓ. The schematic represents a local portion of a deep formation; its upper and lower faces do not represent a free ground surface.

Taking the initial stress-equilibrium state as the reference, let u denote the incremental displacement and s_ℓ the incremental stress in layer ℓ. In the local plane-strain cross-section, $u = (u_y, u_z)$, with the governing relations

$$\nabla \cdot \mathbf{s}_\ell = \mathbf{0},\ \mathbf{s}_\ell = 2G_\ell \boldsymbol{\varepsilon} + \lambda_\ell \mathrm{tr}(\boldsymbol{\varepsilon})\mathbf{I},\ \boldsymbol{\varepsilon} = \frac{\nabla \mathbf{u} + (\nabla \mathbf{u})^{\mathrm{T}}}{2} \tag{12}$$

Here, $G_\ell = E_\ell/[2(1+\nu_\ell)]$ and $\lambda_\ell = E_\ell\nu_\ell/[(1+\nu_\ell)(1-2\nu_\ell)]$. The plane-strain conditions are $u_x = 0$ and $\partial/\partial_x = 0$, while the constitutive calculation retains the out-of-plane stress induced by this constraint. Far-field conditions require perturbations relative to the initial state to decay; the influence of boundary truncation should be checked by enlarging the computational domain. Net pressure p_n is applied to the fracture faces to avoid counting in situ stress twice.

Following linear interface compliance theory [13] and its application to layered fracture calculations [14], an intact bedding interface is represented by continuity of normal displacement and a linear tangential spring. With a common interface-normal convention, the interface relations are

$$[u_z]_{\Gamma_\ell} = 0,\ \tau_y = k_{t,\ell}[u_y]_{\Gamma_\ell},\ [sn]_{\Gamma_\ell} = \mathbf{0} \tag{13}$$

Square brackets denote the value on the upper side minus that on the lower side of the interface, and $k_{t,\ell}$ has units of Pa/m. The bedding displacement jump and the opening displacement between the two hydraulic fracture faces occur at different locations and have different physical meanings. Figure 3 shows the two tangential components of a general three-dimensional interface; the present local y–z plane-strain model retains only the y-component.

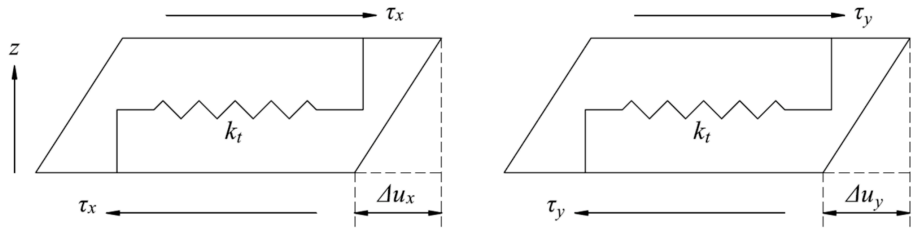


Figure 3. Two components of a linear tangential elastic interface. (**a**) Tangential traction τ_x and relative displacement Δu_x in the x-direction; (**b**) tangential traction τ_y and relative displacement Δu_y in the *y*-direction. The stiffness k_t relates tangential traction to unit displacement jump, and the springs illustrate the linear traction–displacement relation. The present local *y*–*z* plane-strain model solves only the tangential response in (**b**); (**a**) illustrates general three-dimensional interface kinematics. Inclination schematically represents deformation, while normal displacement remains continuous across the interface.

For the cross-sectional domain Ω_ℓ of layer ℓ and its internal interface Γ_ℓ, let v be a test function satisfying homogeneous outer-boundary constraints and $[v_z] = 0$. Bulk elasticity and interface springs together give the weak form:

$$\sum_{\ell=1}^{N}\int_{\Omega_\ell}\boldsymbol{\varepsilon}(\mathbf{v}):\mathbf{D}_\ell:\boldsymbol{\varepsilon}(\mathbf{u})\,d\Omega + \sum_{\ell=1}^{N-1}\int_{\Gamma_\ell}k_{t,\ell}[v_y][u_y]\,d\Gamma = \int_{\Gamma_f}p_n[v_y]_f\,d\Gamma \tag{14}$$

Here, D_ℓ is the plane-strain elasticity tensor, Γ_f denotes the fracture line segments in the cross-section, and $[v_y]_f$ is the virtual displacement difference between the two fracture faces. The interface integral in Equation (14) covers only bedding portions not yet cut by the main fracture. The resulting displacements give the fracture aperture and elastic energy per unit interface area:

$$w = [u_y]_f,\ U_{t,\ell} = \frac{1}{2}k_{t,\ell}[u_y]^2_{\Gamma_\ell} \tag{15}$$

The weak form defines how pressure affects aperture: pressure changes rock displacements, interface stiffness modifies the overall elastic response, and aperture subsequently enters the fluid storage and flow calculations. Appendix A provides the matrix discretiza-

tion subject to normal continuity. Bedding portions not yet cut by the main fracture are represented as interfaces with continuous normal displacement and linear tangential elasticity. Their tangential displacement is a recoverable relative shear deformation induced by loading and recovers along the same linear relation upon unloading; $U_{t,\ell}$ is recoverable stored energy. The model does not include frictional yielding, residual shear offset, interface damage, or fluid transport in branches along bedding. When the main fracture crosses an interface, the fractured portion is removed from the spring integration domain. This treatment describes main-fracture formation and the elastic response of the remaining interface, rather than damage evolution along bedding.

These assumptions apply when the focus is on interlayer shear compliance at small deformation, with normal debonding and irreversible slip not explicitly modeled. Describing bedding opening, frictional slip, or fracture deflection along an interface requires the corresponding normal-fracture, frictional constitutive, or path-competition relations [15,17,21], together with updated fluid-partitioning conditions.

2.5. Fluid Conservation and Lateral Front Closure

Integrating the local Poiseuille flux over the actual aperture profile gives the volumetric flow rate along x in one fracture wing [3,10]:

$$q(x,t) = -\frac{1}{\mu'}\frac{\partial p_f}{\partial x}\int_{-h/2}^{h/2} w^3(x,z,t)dz \tag{16}$$

Cross-sectional fluid storage and transport satisfy

$$\frac{\partial A}{\partial t} + \frac{\partial q}{\partial x} + q_{\text{loss}} = 0 \tag{17}$$

Here, q_{loss} is the volumetric loss rate per unit horizontal length, with units of m^2/s. It is set to zero in the reference problem without leakoff. If leakoff is included, a consistent description should be used for the baseline and modified schemes. An independently prescribed empirical flow-rate distribution cannot replace the conservation equation. Let Q_f denote the injection rate allocated to a complete two-wing fracture. The inlet and front conditions are

$$q(0,t) = \frac{Q_f(t)}{2},\ A(L(t),t) = 0,\ q(L(t),t) = 0 \tag{18}$$

At a moving front with no fluid lag or additional tip fluid sink, the fluid particle velocity equals the front speed. The limit approached from inside the fracture provides the kinematic closure:

$$\frac{dL}{dt} = \lim_{x\to L(t)^-}\frac{q(x,t)}{A(x,t)} \tag{19}$$

This limit must be evaluated using a consistent near-front discretization rather than direct substitution of the tip values, which gives $0/0$. The local elastic description used here applies to a P3D approximation dominated by lateral viscous effects. If lateral fracture toughness is significant, it must be treated consistently with nonlocal elasticity and the corresponding tip asymptotes [11,12]. The relation in Equation (19) alone does not incorporate a complete lateral-toughness correction.

For a two-wing fracture without leakoff and with negligible wellbore storage, integral conservation gives

$$2\int_0^{L(t)} A(x,t)\,dx = V_f(0) + \int_0^t Q_f(\tau)\,d\tau \tag{20}$$

The stage injection rate equals the sum of the rates allocated to all active fractures. Assigning the total stage fluid volume directly to one fracture is an additional assumption that must be stated explicitly.

2.6. Vertical Propagation and Layer-Crossing Conditions

During propagation within a homogeneous layer, where a mode I tip description applies, the no-recession condition can be expressed as

$$V \geq 0, K_{\text{eff}} - K_{\text{I}} \geq 0, V(K_{\text{eff}} - K_{\text{I}}) = 0 \tag{21}$$

This condition allows tip arrest. During propagation at a positive speed, the tip driving force equals the sum of material fracture toughness and equivalent viscous resistance. For the reference problem with perfectly bonded interfaces, uniform elastic modulus, and symmetric stress barriers, substituting Equation (1) into the weight-function expression gives

$$K_{\text{I}} = \left[p_{\text{f}} - \sigma_1 - \frac{2\Delta\sigma}{\pi}\theta_h\right]\sqrt{\frac{\pi h}{2}},\ \theta_h = \arccos\left[\min(1, \frac{H_{\text{p}}}{h})\right] \tag{22}$$

The pressure satisfying the condition for continued vertical propagation at a prescribed h is therefore

$$p_{\text{f,c}} = \sigma_1 + \frac{2\Delta\sigma}{\pi}\theta_h + \frac{K_{\text{IC}} + r}{\sqrt{\pi h/2}} \tag{23}$$

This relation separates the contributions of in situ stress, the stress barrier, and equivalent fracture resistance. At fixed geometry and other parameters, $\partial_{\text{pf,c}}/\partial \text{r} = 1/\sqrt{(\pi \text{h}/2)} > 0$; thus, greater additional resistance raises the pressure required to reach that fracture height. This conditional result for the reference problem does not imply that fracture height must decrease by the same proportion in every coupled case with a fixed injection rate. For compliant bedding interfaces, the driving force must be recalculated from the layered elastic solution, and Equation (23) cannot be applied directly as a universal multilayer penetration formula.

Geometric layer crossing requires the front to pass the specified interface position. The number of interfaces within the currently fractured interval is defined as

$$N_\Gamma(x,t) = \sum_{\ell=1}^{N-1} 1[-h(x,t)/2 < z_\ell < h(x,t)/2] \tag{24}$$

The indicator function equals 1 when the condition holds and 0 otherwise. A front that has only reached an interface is not counted as having penetrated it. Assessment also requires the actual interface elevations, front positions, and feasible propagation conditions beyond the interface. For models that explicitly compare penetration and deflection paths, an energy-competition approach [15,16] gives

$$\eta_{\text{p}} = \frac{G_{\text{p}}}{G_{\text{pc}}},\ \eta_{\text{d}} = \frac{G_{\text{d}}}{G_{\text{dc}}} \tag{25}$$

Here, G_{p} and G_{d} are the energy release rates for the two candidate paths, and the denominators are their respective critical values. Path selection also depends on material mismatch, mixed-mode fracture resistance, and fluid partitioning. The present elastic interface with continuous normal displacement cannot generate a fracture branch that opens along bedding. The criterion in Equation (25) therefore identifies quantities that an extended model would need to compare, rather than a deflection algorithm implemented in this study.

2.7. Coupled Discretization and Solution Procedure

Equations (14), (16) and (17) connect the elastic interface response to fluid transport, while Equations (10), (11) and (21) govern updates of the symmetric vertical fronts. For horizontal control volume i, the conservation residual under backward time discretization is

$$R_i = \frac{A_i^{n+1} - A_i^n}{\Delta t} + \frac{q_{i+1/2}^{n+1} - q_{i-1/2}^{n+1}}{\Delta x_i} + q_{\mathrm{loss},i}^{n+1} \tag{26}$$

The control-volume face flux in Equation (26) is calculated from the aperture-cubed integral in Equation (16) and the pressure difference between adjacent control volumes. Each time step is initialized using the pressure, fracture height, and lateral front position at the previous converged time. For the current geometry, the layered elastic matrices in Appendix A are assembled and normal continuity is imposed to solve for aperture, interfacial displacement, and tip driving force. Cross-sectional area and flux are then calculated, the vertical speed is updated using Equation (11), and the additional toughness is updated using Equation (10). Pressure, fracture height, and front position are iterated jointly through mass conservation and propagation conditions, with the lateral front updated according to Equation (19). When the main fracture crosses an interface, the fractured portion is removed from the interface spring integration domain.

The solution procedure controls the scalar root-finding error separately from the coupled iteration error within each time step [5,8]. When F = 0, r = 0 is assigned directly. When F > 0, bisection is performed over [0, $F^{1/6}$] for the B and F values specified by the current outer iteration. The scalar solve terminates when both the absolute equation residual normalized by F and the root-bracket width normalized by $F^{1/6}$ are no greater than 10^{-8}. For B = 0, the root is the upper endpoint $F^{1/6}$. The unique nonnegative-root property established in Appendix B ensures the validity of this bracket.

The outer loop uses successive iteration with a relaxation factor of 0.5 to update pressure and front position. Elastic aperture, interfacial displacement, cross-sectional flux, and additional toughness are recalculated from the updated pressure and geometry. Iterative changes in pressure, aperture, and front position are normalized by positive characteristic scales with the corresponding dimensions. Once all normalized changes are no greater than 10^{-5} and the normalized mass-conservation residual in Equation (26) is no greater than 10^{-6}, the front-propagation conditions in Equation (21) are checked. For an advancing front, the tip driving force must balance the effective fracture resistance; for an arrested front, the driving force must not exceed that resistance. The calculation advances to the next time step only when the variable-update, conservation-residual, and front conditions are all satisfied.

The outer iteration limit is 50 iterations per time step. If convergence is not reached within this limit, the time-step size is halved and the calculation restarts from the previous converged time. For zero leakoff and negligible wellbore storage, the cumulative injected volume is checked against the stored fracture-fluid volume using Equation (20). These settings were used to solve the original cases; Section 3 organizes and reanalyzes the existing end-of-treatment results.

3. Case Data and Parameter Comparisons

3.1. Data Scope and Evaluation Metrics

The cases are taken from stage 8 of an anonymized sidetracked horizontal well in the Sichuan Basin, designated Well A. The well has a measured depth of 5720.00 m, a true vertical depth of 4069.55 m, and a horizontal-section length of 1520.00 m. The target interval contains interbedded shale, argillaceous sandstone, and siltstone. This section

organizes and reanalyzes existing end-of-treatment case results for this stage. The original solution settings are given in Section 2.7, and the sources and adopted values of treatment and material parameters are listed in Table 1.

Table 1. Treatment and material parameters for stage 8 of Well A, with their sources and adopted values.

Parameter	Value	Source and Basis for the Adopted Value
Minimum horizontal stress in the injection layer, σ_1	42.6 MPa	Representative value from the in situ stress interpretation for the injection layer.
Minimum horizontal stress in the bounding layers, σ_2	47.3 MPa	Representative interpreted stress for the bounding layers; the same value is used above and below the injection layer.
Stress contrast, $\Delta\sigma$	4.7 MPa	Calculated as $\sigma_2 - \sigma_1$.
Young's modulus, E	24.8 GPa	Representative value from the rock-mechanics interpretation for the target interval.
Poisson's ratio, ν	0.23	Rock-mechanics interpretation value paired with Young's modulus.
Matrix fracture toughness, K_{IC}	0.72 MPa·m$^{1/2}$	Value prescribed in the original case.
Dynamic viscosity, μ	3 mPa·s	From fracturing-fluid property data; treated as constant in the calculation.
Stage injection rate	10 m^3/min	From treatment records; used as a constant stage-level injection rate.
Injection duration	140 min	Injection duration recorded for the treatment.
Total stage fluid volume	1400 m^3	Calculated as injection rate multiplied by injection duration.
Tangential stiffness of the bedding interface, $k_{t,\ell}$	2.2 GPa/m	Recorded value from the original case, used as the tangential stiffness in Equation (13).

Note: $k_{t,\ell}$ is the tangential stiffness of bedding interface ℓ, relating tangential traction to tangential displacement jump in Equation (13). Its unit is Pa/m; the tabulated value of 2.2 GPa/m equals 2.2×10^9 Pa/m. Normal displacement remains continuous across the interface. Injection rate and total fluid volume are stage-level parameters.

The stress parameters in Table 1 are representative values selected for the injection and bounding layers from the in situ stress interpretation for this well; both upper and lower bounding layers are assigned σ_2. Young's modulus and Poisson's ratio are paired rock-mechanics interpretation values for the target interval and are used as equivalent linear elastic properties. Dynamic viscosity is taken from fracturing-fluid property data, whereas injection rate and duration are taken from treatment records. Viscosity and injection rate are treated as constant in the model. Matrix fracture toughness and tangential interface stiffness retain the values prescribed in the original case and enter the front-propagation condition and the elastic interface relation in Equation (13), respectively. Stress contrast and total stage fluid volume are calculated from the parameters listed in the table.

The parameters C and C_2 in Section 2.3 are literature calibration parameters for the dynamic apparent-toughness update. Tables 2 and 3 group cases by prescribed additional toughness to compare end-of-treatment fracture geometry and interfacial displacement; these comparisons are discussed separately from the dynamic update in Equation (10). The field-interpreted height range of 52–58 m and half-length of 172 m provide geometry comparison references and are listed separately from the model inputs.

Table 2. Relationship between prescribed additional toughness and maximum fracture height in the first dataset.

Additional Apparent Toughness (MPa·m$^{1/2}$)	Maximum Fracture Height (m)
0	86.2
0.4	72.5
0.8	58.1
1.2	43.6
1.6	33.4

Table 3. Fracture geometry and interfacial displacement at 140 min for the second set of prescribed-toughness cases.

Case	Additional Toughness (MPa·m$^{1/2}$)	Average Fracture Height (m)	Fracture Half-Length (m)	Maximum Tangential Displacement (mm)
1	0.1	71.2	207	0.41
2	0.3	60.5	189	0.67
3	0.5	52.1	174	0.93
4	0.7	43.7	161	1.26

The average and maximum fracture heights are defined as

$$\overline{h}(t) = \frac{1}{L(t)} \int_0^{L(t)} h(x,t)\, \mathrm{d}x\,, h_{max}(t) = max_{0 \le x \le L(t)} h(x,t) \tag{27}$$

Average and maximum fracture heights in the data are discussed separately and are not used interchangeably. The field-interpreted fracture height is 52–58 m, and the half-length is 172 m. The former is an interpreted range rather than a statistical confidence interval. For a specified scalar reference value, the descriptive relative deviation is

$$e_X = \frac{|X_{\text{case}} - X_{\text{ref}}|}{X_{\text{ref}}} \times 100\% \tag{28}$$

The height-range midpoint of 55 m is used only as a common calculation reference and is not treated as an error-free true fracture height.

3.2. Fracture Geometry Comparison with Field Interpretations

Table 4 retains the labels "conventional P3D" and "modified P3D" from the existing cases. The conventional scheme gives a fracture height of 74.3 m, exceeding the upper bound of the interpreted range by 16.3 m; the modified value of 55.6 m lies within that range. Relative to its midpoint of 55 m, the descriptive deviations are 35.09% and 1.09%, respectively.

Table 4. Comparison of reported end-of-treatment case values with field interpretations.

Metric	Field Interpretation	Conventional P3D	Modified P3D
Average fracture height (m)	52–58	74.3	55.6
Deviation from the 55 m midpoint (%)	/	35.09	1.09
Within the interpreted height range	/	No	Yes
Fracture half-length (m)	172	216	178
Half-length relative deviation (%)	/	25.58	3.49

The modified half-length of 178 m differs from the field-interpreted value of 172 m by 6 m, giving a relative deviation of 3.49%. The conventional half-length is 216 m, with a relative deviation of 25.58%. Figure 4 compares the fracture geometry from both schemes with the field interpretations, using the interpreted range of 52–58 m for fracture height and the interpreted scalar value of 172 m for half-length. For the stage examined, the modified height of 55.6 m lies within the interpreted range, and its half-length deviation is smaller than that of the conventional scheme. The modified scheme therefore agrees more closely with the field-interpreted fracture geometry in this case.

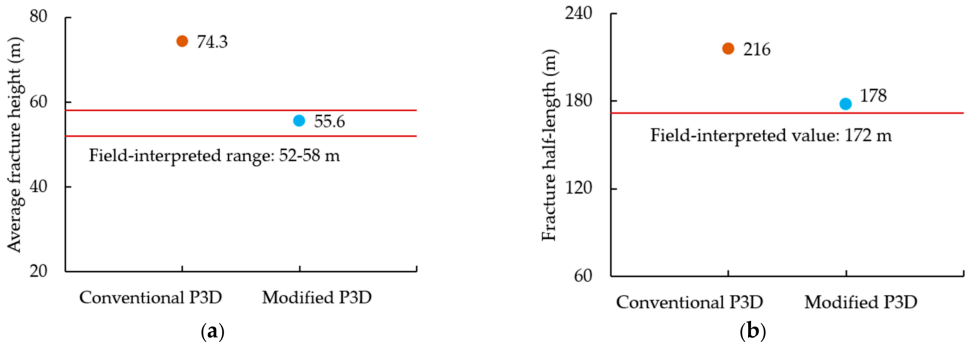


Figure 4. Comparison of end-of-treatment fracture geometry with field interpretations for stage 8. (**a**) Average fracture height; the two red horizontal solid lines mark the lower and upper bounds of the interpreted range, 52 and 58 m. (**b**) Fracture half-length; the red horizontal solid line marks the interpreted value of 172 m. Orange-red and blue circles denote the conventional and modified P3D schemes, respectively, and the numbers beside the points give their values. Data are from Table 4; the height range is a field-interpreted interval.

3.3. Parameter Trends at Prescribed Additional Toughness

The first dataset covers additional apparent toughness values of 0–1.6 MPa·m$^{1/2}$, over which the maximum fracture height decreases from 86.2 to 33.4 m, a reduction of 61.25% (Table 2). Zero additional toughness removes only the equivalent viscous resistance; it does not set the matrix fracture toughness to zero. The maximum end-of-treatment height alone does not determine the number of crossed interfaces. Assessment using Equation (24) also requires the actual interface elevations and the fracture profile along the propagation direction.

The second dataset corresponds to a treatment duration of 140 min and includes four prescribed additional-toughness values (Table 3). As additional toughness increases from 0.1 to 0.7 MPa·m$^{1/2}$, the average fracture height decreases from 71.2 to 43.7 m, a reduction of 38.62%, and the fracture half-length decreases from 207 to 161 m, a reduction of 22.22%. The maximum tangential interfacial displacement increases from 0.41 to 1.26 mm, approximately 3.07 times its initial value.

Figure 5 shows that, over the listed parameter range, greater additional toughness corresponds to smaller average fracture height and half-length and greater maximum tangential interfacial displacement. This displacement is the recoverable jump defined by the linear elastic relation in Equation (13). It reflects interlayer shear-deformation adjustment rather than frictional slip or interface damage. Table 3 compares end-of-treatment responses at different prescribed additional toughness values.

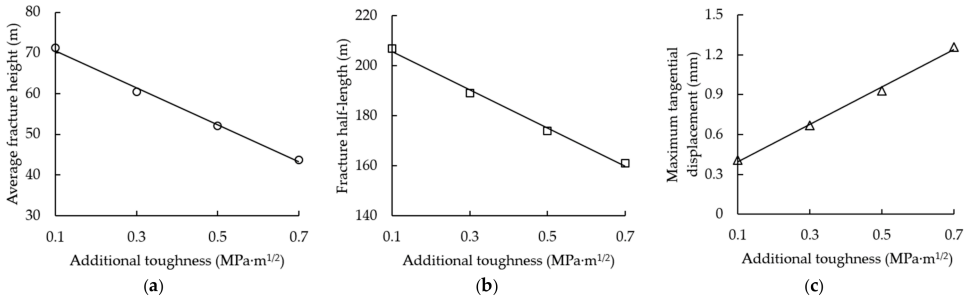


Figure 5. End-of-treatment responses at 140 min for prescribed additional toughness. (**a**) Average fracture height, shown as open circles; (**b**) fracture half-length, shown as open squares; (**c**) maximum tangential interfacial displacement, shown as open triangles. The symbols correspond to the four cases in Table 3. The horizontal axis in each panel is prescribed additional toughness, and connecting lines illustrate trends between the discrete data points. The displacement in (**c**) is the recoverable elastic displacement jump of the linear interface.

4. Discussion

4.1. Roles of Vertical Propagation Resistance and Interlayer Deformation

Apparent toughness and interface compliance act at different stages of fracture propagation. The former represents the viscous effects of vertical flow as an equivalent front resistance, whose magnitude depends on the propagation state and matching length [11]. The latter changes the cross-sectional elastic response through relative deformation between layers. Their coupling therefore reflects the interaction between propagation resistance and deformation capacity: interface compliance adjusts the pressure-induced aperture distribution, aperture changes fluid storage and transport, and changes in pressure and front speed further affect the additional apparent toughness.

The relation in Equation (23) shows that, at fixed geometry in the reference problem, increasing additional toughness raises the pressure required for continued vertical propagation. At a fixed injection rate, fracture height, length, and aperture jointly determine fluid storage and flow. Changes in height and half-length must therefore be interpreted together with pressure and fluid volume balance. The end-of-treatment trends in Tables 2 and 3 describe geometric responses within the listed parameter ranges.

Bedding compliance modifies the cross-sectional elastic response through the linear relation between tangential traction and relative displacement [13,14]. The increase in maximum tangential displacement in Table 3 indicates greater local recoverable shear deformation. Total energy stored at the interface also depends on stiffness and the spatial distribution of displacement. This elastic deformation has a different physical meaning from dissipation caused by frictional slip or damage.

4.2. Engineering Interpretation of Field Comparisons and Fluid Volume Balance

The interpreted height range and scalar half-length are compared using interval inclusion and relative deviation, respectively. For both metrics, the modified scheme more closely matches the field interpretation for the stage studied. Manjunath et al. [24] noted that microseismic events can include shear-failure responses in regions not directly connected to the injected fluid; the event distribution can therefore differ from the extent of the fluid-filled fracture. Their multistage fracturing experiments and modeling with PMMA specimens demonstrated the complementary value of injection- and monitoring-well pressure information for interpreting fracture geometry. This finding indicates that field interpretations should be analyzed in light of the physical meaning of the monitoring measurements and fluid volume constraints. Accordingly, this study uses the interpreted

height range and half-length as geometry comparison references and examines the link between fracture dimensions and injected volume through the volume relations below.

Geometric agreement also needs to be interpreted in terms of fluid volume balance. The treatment rate and duration in Table 1 give a total stage injection volume of 1400 m^3. In an idealized scenario with no leakoff and all fluid entering one two-wing fracture, conversion of this volume using the modified half-length and average height gives an equivalent mean aperture of approximately 70.7 mm. This value corresponds to the stated single-fracture allocation assumption and illustrates the scale relationship between stage-level injection volume and individual fracture volume. In multicluster fracturing, the stage injection rate is partitioned among active fractures and contributes to their respective fluid storage and propagation. Cluster-level flow partitioning is therefore an important link between treatment parameters and fracture geometry.

The relationship between fracture height and half-length can be expressed through the volume of a two-wing fracture. Let $\bar{w}$ denote the fracture-area-weighted mean aperture. Then $V_f = 2L\bar{h}\bar{w}$, where $\bar{h}$ is defined in Equation (27). At the same effective stored fluid volume, simultaneous decreases in height and half-length require an increase in mean aperture. If leakoff, storage, or flow partitioning differs, changes in effective fluid volume must also be included. The geometry trends in Table 3 should therefore be interpreted together with aperture and fluid volume constraints.

4.3. Layer-Crossing Analysis and Model Application

Fracture crossing of layers has both geometric and mechanical aspects. Geometrically, it concerns the relative positions of the front and formation interfaces and the process of crossing them. Mechanically, it concerns the driving forces and corresponding fracture resistances of candidate propagation paths. Combining interface elevations, front positions, and local propagation conditions distinguishes propagation within a layer, arrival at an interface, and crossing of an interface, linking the analysis to the actual layered structure.

The linear tangential interface used here focuses on elastic deformation between layers. Fracture along bedding, frictional slip, and flow into branches involve fracture-path competition, frictional constitutive behavior, and fluid partitioning, respectively [15,17,21]. These mechanisms connect to the present framework through interface tractions, displacement jumps, and local pressure states. Incorporating the corresponding relations would extend the analysis to fracture penetration, deflection, and propagation along bedding.

Section 2.4 and Appendix A allow elastic properties, layer thicknesses, and tangential interface stiffnesses to be specified separately for individual layers, providing a local elastic description of multiple layers with contrasting properties. The apparent-toughness calibration and pressure relation in Equation (23), however, correspond to the stated reference conditions. For formations with pronounced interlayer property contrasts or asymmetric upper and lower stress barriers, the tip driving force should be obtained from the actual layered solution, and the applicability of the apparent-toughness approximation should be assessed.

The model uses a local plane-strain P3D approximation and represents bedding as interfaces with continuous normal displacement and linear tangential elasticity. Frictional slip, interface damage, and fluid branches opening along bedding are not explicitly represented. The field comparison uses end-of-treatment geometry from a single stage in one well, without matching complete pressure–time histories. The results therefore primarily describe geometric responses and parameter trends under the specified conditions.

5. Conclusions

(1) A coupled P3D framework incorporating apparent fracture toughness and elastic compliance of bedding interfaces was developed. The weak formulation of layered elasticity, fluid conservation, and front-update conditions establish the computational links among fracture pressure, aperture, interfacial displacement, and propagation speed.

(2) Under calibration for symmetric stress barriers, the implicit additional apparent-toughness relation can be transformed into an algebraic equation with a unique nonnegative root. For the perfectly bonded reference conditions, a vertical propagation pressure relation was derived at a prescribed fracture height, establishing the conditional relationship between increased additional resistance and higher propagation pressure.

(3) In the end-of-treatment comparison for the stage examined, the modified fracture height of 55.6 m lies within the field-interpreted range of 52-58 m. The half-length of 178 m has a relative deviation of 3.49% from the interpreted value of 172 m. Both geometric metrics from the modified scheme are closer to the field interpretations than those from the conventional scheme.

(4) Increasing prescribed additional toughness from 0.1 to 0.7 MPa·m$^{1/2}$ corresponds to decreases of 38.62% and 22.22% in average fracture height and half-length, respectively, and an increase in maximum tangential interfacial displacement from 0.41 to 1.26 mm. These end-of-treatment data show the associated trends in additional resistance, fracture dimensions, and recoverable elastic deformation between layers. Joint interpretation of fracture height and half-length requires consistency with aperture and effective fluid volume constraints.

Author Contributions: Conceptualization, L.L. and H.Y.; methodology, L.L. and H.Y.; investigation, L.L., H.Y. and D.L.; resources, H.Y.; data curation, L.L. and D.L.; writing—original draft preparation, L.L. and H.Y.; writing—review and editing, L.L. and H.Y.; funding acquisition, H.Y. All authors have read and agreed to the published version of the manuscript.

Funding: This research was funded by the Sinopec Research Institute of Petroleum Engineering, grant number G5800-18-ZS-KFZY-006.

Data Availability Statement: The numerical values used for the comparisons are presented in the article.

Conflicts of Interest: The authors declare no conflicts of interest. This research was supported by the Open Fund of the State Key Laboratory of Shale Oil and Gas Enrichment Mechanisms and Effective Development. The funder was not involved in the study design, collection, analysis, interpretation of data, the writing of this article or the decision to submit it for publication.

Appendix A. Matrix Discretization of the Layered Elastic Weak Form

A displacement approximation u = N_{ℓ}d, compatible with the fracture and interfaces, is used in each layer. Separate displacement degrees of freedom are assigned to the two sides of each interface to allow tangential jumps. Let B_{ℓ} be the strain–displacement matrix and $J_{t,\ell}$ the interpolation matrix for the tangential interface jump. The bulk and interface stiffness matrices are

$$\mathbf{K}_{b} = \sum_{\ell=1}^{N} \int_{\Omega_{\ell}} \mathbf{B}_{\ell}^{T} \mathbf{D}_{\ell} \mathbf{B}_{\ell} \, d\Omega, \; \mathbf{K}_{t} = \sum_{\ell=1}^{N-1} \int_{\Gamma_{\ell}} \mathbf{J}_{t,\ell}^{T} k_{t,\ell} \mathbf{J}_{t,\ell} \, d\Gamma \tag{A1}$$

Pressure can be represented using fracture-face nodes or piecewise basis functions N_{p}. Let J_{f} map nodal displacements to fracture-face opening. The consistent surface-load matrix is

$$\mathbf{F}_{p} = \int_{\Gamma_{f}} \mathbf{J}_{f}^{T} \mathbf{N}_{p} \, d\Gamma, \; \mathbf{f} = \mathbf{F}_{p} \mathbf{p}_{n} \tag{A2}$$

Normal continuity and homogeneous displacement constraints on the outer boundary are written as $C_d = 0$. Let P be a full-column-rank matrix whose columns span the admissible displacement space, such that $C_P = 0$, and set $d = Pa$. Substitution into the weak form gives the equations after constraint elimination:

$$\mathbf{K}_r\mathbf{a} = \mathbf{P}^T\mathbf{F}_p\mathbf{p}_n,\ \mathbf{K}_r = \mathbf{P}^T(\mathbf{K}_b + \mathbf{K}_t)\mathbf{P} \tag{A3}$$

When the elastic constants satisfy stability conditions, tangential stiffnesses are positive, rigid-body degrees of freedom are removed, and the constraints are independent, K_r is symmetric positive definite. Fracture aperture and tangential interfacial displacement are extracted from the displacement solution as

$$\mathbf{w} = \mathbf{J}_f\mathbf{P}\mathbf{K}_r^{-1}\mathbf{P}^T\mathbf{F}_p\mathbf{p}_n,\ \Delta\mathbf{u}_{t,\ell} = \mathbf{J}_{t,\ell}Pa \tag{A4}$$

These relations give the complete discrete mapping from pressure to aperture. Implementation should solve the linear system rather than explicitly calculate a matrix inverse. Changes in geometry require consistent updates of integration domains, fractured surfaces, and the corresponding matrices.

The discrete elastic energy is

$$U_e = \frac{1}{2}\mathbf{d}^T\mathbf{K}_b\mathbf{d} + \frac{1}{2}\mathbf{d}^T\mathbf{K}_t\mathbf{d} \tag{A5}$$

As $k_{t,\ell}$ increases while elastic energy remains bounded, the corresponding tangential displacement jump tends to zero. Together with normal continuity, this recovers a perfectly bonded interface. As $k_{t,\ell}$ approaches zero, the interfacial shear traction tends to zero, but additional rigid-body motions may arise, requiring checks on constraints and uniqueness. These limits provide checks on interface compliance; an arbitrarily large stiffness value alone does not establish numerical convergence.

Appendix B. Dimensional Consistency and Uniqueness of the Apparent-Toughness Equation

From Equation (8), the product of $(E')^{2/3}$, $(\mu')^{1/3}$, $V^{1/3}$, and $d^{1/6}$ has units of Pa·m$^{1/2}$. In Equation (10), B has the same units as r and F has units of r^6, so all terms are dimensionally consistent. Let $f(r) = r^6 + Br^5 - F$. Then,

$$\xi^6 + \zeta\xi^5 = 1,\ 0 < \xi \le 1,\ \frac{d\xi}{d\zeta} = -\frac{\xi}{6\xi + 5\zeta} < 0 \tag{A6}$$

For $V > 0$, $f(0) = -F < 0$ and $f(F^{1/6}) = BF^{5/6} \ge 0$. Continuity and strict monotonicity therefore establish a unique positive root. For $V = 0$, the unique nonnegative root of $r^5(r + B) = 0$ is zero. Accordingly, a positive viscous correction inde

$$A = \frac{2\pi p_n a^2}{E'},\ \int_{-a}^{a} w^3(z)\,dz = \frac{24\pi p_n^3 a^4}{(E')^3} \tag{A7}$$

ndent of speed should not be retained when the reference speed V is zero.

For $F > 0$, introducing $r_0 = F^{1/6}$, $\xi = r/r_0$, and $\zeta = B/r_0$ reduces the root equation to

$$\xi^6 + \zeta\xi^5 = 1,\ 0 < \xi \le 1,\ \frac{d\xi}{d\zeta} = -\frac{\xi}{6\xi + 5\zeta} < 0 \tag{A8}$$

This relation shows that, at fixed r_0, increasing the barrier correction parameter ζ decreases the dimensionless additional toughness $\xi = r/r_0$. The stress barrier also contributes

to the tip driving-force calculation through the elastic loading. Vertical propagation conditions are jointly determined by material fracture toughness, additional apparent toughness, and stress-barrier loading. At fixed h and B, r increases with positive propagation speed V. During time evolution, fracture height, propagation speed, and the corresponding barrier term jointly control the additional toughness, whose evolution is determined by the coupled state at each instant.

Integrating the area and hydraulic conductance of the perfectly bonded reference solution gives another set of testable relations:

$$A = \frac{2\pi p_n a^2}{E'}, \int_{-a}^{a} w^3(z)\,\mathrm{d}z = \frac{24\pi p_n^3 a^4}{(E')^3} \tag{A9}$$

These relations follow directly by integrating Equation (5) and provide checks on area and flow discretization. They do not apply to general aperture distributions with stress discontinuities or compliant interfaces.

References

1. Zhao, W.; Hu, S.; Hou, L.; Yang, T.; Li, X.; Guo, B.; Yang, Z. Types and resource potential of continental shale oil in China and its boundary with tight oil. *Pet. Explor. Dev.* **2020**, *47*, 1–11. [CrossRef]
2. Warpinski, N.R.; Teufel, L.W. Influence of geologic discontinuities on hydraulic fracture propagation (includes associated papers 17011 and 17074). *J. Pet. Technol.* **1987**, *39*, 209–220. [CrossRef]
3. Adachi, J.; Siebrits, E.; Peirce, A.; Desroches, J. Computer simulation of hydraulic fractures. *Int. J. Rock Mech. Min. Sci.* **2007**, *44*, 739–757. [CrossRef]
4. Detournay, E. Mechanics of hydraulic fractures. *Annu. Rev. Fluid Mech.* **2016**, *48*, 311–339. [CrossRef]
5. Lecampion, B.; Bunger, A.; Zhang, X. Numerical methods for hydraulic fracture propagation: A review of recent trends. *J. Nat. Gas. Sci. Eng.* **2018**, *49*, 66–83. [CrossRef]
6. Settgast, R.R.; Fu, P.; Walsh, S.D.C.; White, J.A.; Annavarapu, C.; Ryerson, F.J. A fully coupled method for massively parallel simulation of hydraulically driven fractures in 3-dimensions. *Int. J. Numer. Anal. Methods Geomech.* **2017**, *41*, 627–653. [CrossRef]
7. Moës, N.; Belytschko, T. Extended finite element method for cohesive crack growth. *Eng. Fract. Mech.* **2002**, *69*, 813–833. [CrossRef]
8. Peirce, A.; Detournay, E. An implicit level set method for modeling hydraulically driven fractures. *Comput. Methods Appl. Mech. Eng.* **2008**, *197*, 2858–2885. [CrossRef]
9. Damjanac, B.; Cundall, P. Application of distinct element methods to simulation of hydraulic fracturing in naturally fractured reservoirs. *Comput. Geotech.* **2016**, *71*, 283–294. [CrossRef]
10. Adachi, J.I.; Detournay, E.; Peirce, A.P. Analysis of the classical pseudo-3D model for hydraulic fracture with equilibrium height growth across stress barriers. *Int. J. Rock Mech. Min. Sci.* **2010**, *47*, 625–639. [CrossRef]
11. Dontsov, E.V.; Peirce, A.P. An enhanced pseudo-3D model for hydraulic fracturing accounting for viscous height growth, non-local elasticity, and lateral toughness. *Eng. Fract. Mech.* **2015**, *142*, 116–139. [CrossRef]
12. Dontsov, E.V.; Peirce, A.P. Comparison of toughness propagation criteria for blade-like and pseudo-3D hydraulic fractures. *Eng. Fract. Mech.* **2016**, *160*, 238–247. [CrossRef]
13. Schoenberg, M. Elastic wave behavior across linear slip interfaces. *J. Acoust. Soc. Am.* **1980**, *68*, 1516–1521. [CrossRef]
14. Peirce, A.P.; Gu, H.; Siebrits, E. Uniform asymptotic Green's functions for efficient modeling of cracks in elastic layers with relative shear deformation controlled by linear springs. *Int. J. Numer. Anal. Methods Geomech.* **2009**, *33*, 285–308. [CrossRef]
15. He, M.Y.; Hutchinson, J.W. Crack deflection at an interface between dissimilar elastic materials. *Int. J. Solids Struct.* **1989**, *25*, 1053–1067. [CrossRef]
16. Yang, H.Q.; Zhao, H. Investigation of the behavior of vertical fracture penetration/deflection at the interface between coal seam and mudstone layers. *Strength Fract. Complex.* **2019**, *12*, 1–13. [CrossRef]
17. Zhang, X.; Jeffrey, R.G. Reinitiation or termination of fluid-driven fractures at frictional bedding interfaces. *J. Geophys. Res. Solid Earth* **2008**, *113*, B08416. [CrossRef]
18. Lu, Q.; EI-Fayoumi, A.; Adachi, J.; Zaki, K.; Bunger, A. Laboratory demonstration of the impact of weak interfaces and layered rock properties on hydraulic fracture containment and height growth. *Geomech. Geophys. Geo-Energy Geo-Resour.* **2023**, *9*, 113. [CrossRef]
19. Zeng, Q.; Bo, L.; Li, Q.; Sun, J.; Yao, J. Numerical investigation of hydraulic fracture propagation interacting with bedding planes. *Eng. Fract. Mech.* **2023**, *291*, 109575. [CrossRef]

20. Shi, C.; Shentu, J.; Lin, B.; Wei, S.; Jin, Y.; Yoon, J.S. Digital simulation of hydraulic fracturing in laminated shale formation containing varying bedding planes. *Processes* **2025**, *13*, 1017. [CrossRef]
21. Li, S.; Zhang, S.; Zhang, X.; Chen, M.; Li, S.; Zou, Y.; Guo, T.; Zhou, T.; Chen, Z. Numerical study of hydraulic fracture propagation coupling frictional bedding planes in shale reservoirs. *Comput. Geotech.* **2025**, *184*, 107298. [CrossRef]
22. Huang, L.; Dontsov, E.; Fu, H.; Lei, Y.; Weng, D.; Zhang, F. Hydraulic fracture height growth in layered rocks: Perspective from DEM simulation of different propagation regimes. *Int. J. Solids Struct.* **2022**, *238*, 111395. [CrossRef]
23. Huang, L.; Liu, J.; Zhang, F.; Dontsov, E.; Damjanac, B. Exploring the influence of rock inherent heterogeneity and grain size on hydraulic fracturing using discrete element modeling. *Int. J. Solids Struct.* **2019**, *176–177*, 207–220. [CrossRef]
24. Manjunath, G.L.; Liu, Z.; Jha, B. Multi-stage hydraulic fracture monitoring at the lab scale. *Eng. Fract. Mech.* **2023**, *289*, 109448. [CrossRef]

Disclaimer/Publisher's Note: The statements, opinions and data contained in all publications are solely those of the individual author(s) and contributor(s) and not of MDPI and/or the editor(s). MDPI and/or the editor(s) disclaim responsibility for any injury to people or property resulting from any ideas, methods, instructions or products referred to in the content.